Supporting Information

Zhang and Dudko 10.1073/pnas.1309101110

SI Text

I. Brownian Dynamics Simulations

A. System with a Single Intermediate. Brownian dynamics simulations were performed on the combined time-dependent potential $G(x,X,t)=G_0(x)+G_L(X-x)+\varkappa(X_0\pm Vt-X)^2/2$, where $\pm$ indicates the stretching/relaxation protocol, $x=x(t)$ is the extension of the molecule, $X=X(t)$ is the extension of the molecule-linker construct, and X_0 is the initial stage-to-cantilever base separation (or trap-to-trap separation). $G_0(x)$ is the intrinsic molecular potential and $G_L(L=X-x)$ is the potential of the linker tethering the molecule to the pulling device; both are detailed below. The spring constant of the pulling device $\varkappa=5$ pN/nm represented an atomic force microscope (AFM) cantilever.

The free-energy profile $G_0(x)$ of the system with a single intermediate (Fig. 3*A*), suitable for running Brownian dynamics simulations, was constructed as follows. The positions and heights of the minima (N, I, U) and the maxima of the free-energy profile were fixed according to the "true" parameters (Table 1), with the origin (0, 0) chosen in state N. These positions were then connected by five piecewise quadratic polynomials according to the following:

$$G_0(x)=\begin{cases}\frac{1}{2}\kappa_{w1}x^2, & x\in[-\infty,x_1];\\ g_{b1}-\frac{1}{2}\kappa_{b1}(x-x_{b1})^2, & x\in[x_1,x_2];\\ g_{w2}+\frac{1}{2}\kappa_{w2}(x-x_{w2})^2, & x\in[x_2,x_3];\\ g_{b2}-\frac{1}{2}\kappa_{b2}(x-x_{b2})^2, & x\in[x_3,x_4];\\ g_{w3}+\frac{1}{2}\kappa_{w3}(x-x_{w3})^2, & x\in[x_4,+\infty],\end{cases} \quad \textbf{[S1]}$$

where $(x_{b1},g_{b1})=(X^{\ddagger}_{NI},\Delta G^{\ddagger}_{NI})$, $(x_{w2},g_{w2})=(x_{b1}+X^{\ddagger}_{IN},g_{b1}-\Delta G^{\ddagger}_{IN})$, $(x_{b2},g_{b2})=(x_{w2}+X^{\ddagger}_{IU},g_{w2}+\Delta G^{\ddagger}_{IU})$, and $(x_{w3},g_{w3})=(x_{b2}+X^{\ddagger}_{UI},g_{b2}-\Delta G^{\ddagger}_{UI})$ are the positions of the barriers and wells (maxima and minima), and κ_{w1}, κ_{w2}, κ_{w3}, κ_{b1}, κ_{b2} are the corresponding stiffnesses (curvatures). The polynomials were matched at positions x_1, x_2, x_3, x_4, where $x_1=X^{\ddagger}_{NI}/2$ and the other x_i's and κ_i's were determined by requiring the derivatives $dG_0(x)/dx$ to be continuous at these matching points.

An anharmonic linker was explicitly accounted for as a worm-like chain with the potential

$$G_L(L)=\frac{k_BT}{L_p}\left[\frac{L_c}{4}\left(1-\frac{L}{L_c}\right)^{-1}-\frac{L}{4}+\frac{L^2}{2L_c}-\frac{L_c}{4}\right], \quad \textbf{[S2]}$$

which can be obtained by integrating the worm-like chain force–extension relation (1). The contour length $L_c=30$ nm and the persistence length $L_p=0.4$ nm represented a polypeptide linker.

The conformational dynamics of the molecule and linker were assumed to be diffusive and governed by the corresponding Langevin equations (2) with a position-dependent diffusion coefficient of the molecule $D_m(x)$:

$$\begin{aligned}\frac{dx}{dt}&=-\frac{D_m(x)}{k_BT}\left[\frac{dG_0(x)}{dx}+\frac{\partial G_L(X-x)}{\partial x}\right]+\frac{dD_m(x)}{dx}+\mathcal{R}_m(t),\\ \frac{dX}{dt}&=-\frac{D_L}{k_BT}\left[\frac{\partial G_L(X-x)}{\partial X}-\varkappa(X_0\pm Vt-X)\right]+\mathcal{R}_L(t),\end{aligned} \quad \textbf{[S3]}$$

where $D_L=5\times10^4$ nm^2/s is the diffusion coefficient of the linker, which is slowed down due to the attachment to the pulling device (e.g., the AFM cantilever) (3). $\mathcal{R}_m(t)$ and $\mathcal{R}_L(t)$ are the Gaussian random forces with zero mean and the corresponding variances $\overline{\mathcal{R}_m(t)\mathcal{R}_m(t')}=2D_m(x(t))\delta(t-t')$ and $\overline{\mathcal{R}_L(t)\mathcal{R}_L(t')}=2D_L\delta(t-t')$.

The position dependence of the diffusion coefficient (Fig. S3, solid line) was modeled as follows:

$$D_m(x)=\frac{10^4}{1+e^{a_1(x-b_1)}}+\frac{10^5}{(1+e^{-a_1(x-b_1)})(1+e^{a_2(x-b_2)})}+\frac{10^6}{1+e^{-a_2(x-b_2)}}, \quad \textbf{[S4]}$$

such that it increased by an order of magnitude upon a transition from state N to state I, and by another order of magnitude upon a transition from state I to state U (4). Parameters $a_1=10$ and $a_2=5$ control the sharpness of the sigmoidal switches, and $b_1=(x_{b1}+x_{w2})/2$ and $b_2=(x_{b2}+x_{w3})/2$ are the locations of the switches, chosen at the inflection points past the first and second barriers. An additional test with an alternative form ($D_m(x)\propto x^3$) of the position dependence of the diffusion coefficient (Fig. S3, dashed line) confirmed the accuracy of the extracted parameters (Table S1 and *Section VI*). The robustness of the proposed method against the position dependence of the diffusion coefficient can be understood as a consequence of the fact that the general mean first-passage time expression (5) involves only the diffusion coefficient of the barrier region. Any significant changes, if present, in the diffusion coefficient have been shown (4) to occur beyond the barrier region and therefore only have a relatively minor effect on the accuracy of the barrier parameters extracted with the proposed method.

Force–extension trajectories were generated by numerically iterating the Langevin equations (Eq. **S3**). Each stretching (relaxation) cycle began with the separation $X_0=8.6$ nm (35.6 nm) sufficiently small (large) such that N (U) was initially the predominantly populated state. One thousand trajectories were generated in each of the stretching and relaxation protocols at four nominal loading rates $\varkappa V=10$, 40, 200, and 1,000 pN/s. The values of the extension $x(t)$ of the molecule and the extension $X(t)$ of the molecule-linker construct were collected at a sampling rate of 20 kHz and recorded after averaging over four points. The force measured by the pulling device, $F(t)=\varkappa(X_0\pm Vt-X(t))$, and the extension of the molecule-linker construct, $X(t)$, were analyzed with the method developed in the main content. The values of the extension of the molecule, $x(t)$, were only used for the test of the effects of missed and misjudged events (details in *Section II*).

B. System with a Cascade of Barriers. Brownian dynamics simulations of the molecule with three intermediates were performed on the combined potential $G(x,t)=G_0(x)+G_L(X-x)+\varkappa(X_0\pm Vt-X)^2/2$ with $\pm$ corresponding to the stretching/relaxation protocol. The intrinsic free-energy profile $G_0(x)$ of the molecule was constructed in a similar way to that of the system with a single intermediate, which is described above. The positions and heights of the minima (N, I_1, I_2, I_3, U) and the maxima of the free-energy profile were fixed according to the "true" parameters (Table S2), with the origin (0, 0) chosen in state N. The locations of the minima and maxima were then connected by eight piecewise cubic polynomials via a straightforward generalization of Eq. **S8** below. A worm-like chain linker with the contour length $L_c=600$ nm and the persistence length $L_p=40$ nm represented a DNA handle. The stiffness of the pulling device $\varkappa=0.2$ pN/nm represented an optical trap.

$$G_2(x)=\begin{cases}\frac{3}{2}\Delta G^{\ddagger}_{NI}\frac{x}{x^{\ddagger}_{NI}}-2\Delta G^{\ddagger}_{NI}\left(\frac{x}{x^{\ddagger}_{NI}}-\frac{1}{2}\right)^3-\frac{1}{4}\Delta G^{\ddagger}_{NI}, & x\in[-\infty,x_1];\\ \frac{3}{2}\Delta G^{\ddagger}_{IN}\frac{x_2-x}{x^{\ddagger}_{IN}}-2\Delta G^{\ddagger}_{IN}\left(\frac{x_2-x}{x^{\ddagger}_{IN}}-\frac{1}{2}\right)^3-\frac{1}{4}\Delta G^{\ddagger}_{IN}+\Delta G^{\ddagger}_{NI}-\Delta G^{\ddagger}_{IN}, & x\in[x_1,x_2];\\ \frac{3}{2}\Delta G^{\ddagger}_{IU}\frac{x-x_2}{x^{\ddagger}_{IU}}-2\Delta G^{\ddagger}_{IU}\left(\frac{x-x_2}{x^{\ddagger}_{IU}}-\frac{1}{2}\right)^3-\frac{1}{4}\Delta G^{\ddagger}_{IU}+\Delta G^{\ddagger}_{NI}-\Delta G^{\ddagger}_{IN}, & x\in[x_2,x_3];\\ \frac{3}{2}\Delta G^{\ddagger}_{UI}\frac{x_4-x}{x^{\ddagger}_{UI}}-2\Delta G^{\ddagger}_{UI}\left(\frac{x_4-x}{x^{\ddagger}_{UI}}-\frac{1}{2}\right)^3-\frac{1}{4}\Delta G^{\ddagger}_{UI}+\Delta G^{\ddagger}_{NI}-\Delta G^{\ddagger}_{IN}+\Delta G^{\ddagger}_{IU}-\Delta G^{\ddagger}_{UI}, & x\in[x_3,+\infty],\end{cases} \quad \text{[S8]}$$

For simplicity, the force from the linker, $\partial G_L(X-x)/\partial X$, was assumed to balance the force from the optical trap, $\varkappa(X_0\pm Vt-X)$, reducing the Langevin equations of the system to the following:

$$\frac{dx}{dt}=-\frac{D_m}{k_BT}\left[\frac{dG_0(x)}{dx}-\varkappa(X_0\pm Vt-X)\right]+\mathcal{R}_m(t), \quad \text{[S5]}$$

where $X(x,t)$ was calculated from $\partial G_L(X-x)/\partial X=\varkappa(X_0\pm Vt-X)$, given the molecular extension x at time t. The effective diffusion coefficient of the molecule was taken to be $D_m=2\times10^4$ nm^2/s.

Each stretching (relaxation) cycle began with the separation $X_0=500$ nm (710 nm) sufficiently small (large) such that N (U) was initially the predominantly populated state. One thousand force–extension curves were generated in each of the stretching and relaxation protocols at four nominal loading rates $\varkappa V=1$, 4, 20, and 100 pN/s. The transition times and forces were recorded directly from the simulations.

C. System with Two Competing Pathways and an Intermediate. Brownian dynamics simulations were performed on the combined potential $G(x,y,t)=G_0(x,y)+\varkappa(X_0\pm Vt-x)^2/2$, with $\pm$ corresponding to the stretching/relaxation protocol.

The 2D free-energy landscape $G_0(x,y)$ in the space of two coordinates, x and y, was designed to contain two transition pathways, one of which featured an intermediate. The pathway $G_1(x)$, located at small values of y and containing no intermediate, and the pathway $G_2(x)$, located at larger values of y and containing an intermediate, were incorporated in the expression for $G_0(x,y)$ as follows:

$$G_0(x,y)=\Delta G^{\ddagger}_B e^{-c\left(\frac{x}{a}-1\right)^2-c\left(\frac{y}{b}-1\right)^2}+\beta^{-1}\left(\frac{y}{b}-1\right)^8+\begin{cases}G_1(x), & y\in[-\infty,b];\\ G_2(x)+[G_1(x)-G_2(x)]e^{-c\left(\frac{y}{b}-1\right)^2}, & y\in[b,+\infty],\end{cases} \quad \text{[S6]}$$

where

$$G_1(x)=\begin{cases}\frac{3}{2}\Delta G^{\ddagger}_{NU}\frac{x}{x^{\ddagger}_{NU}}-2\Delta G^{\ddagger}_{NU}\left(\frac{x}{x^{\ddagger}_{NU}}-\frac{1}{2}\right)^3-\frac{1}{4}\Delta G^{\ddagger}_{NU}, & x\in[-\infty,x_5];\\ \frac{3}{2}\Delta G^{\ddagger}_{UN}\frac{x_6-x}{x^{\ddagger}_{UN}}-2\Delta G^{\ddagger}_{UN}\left(\frac{x_6-x}{x^{\ddagger}_{UN}}-\frac{1}{2}\right)^3-\frac{1}{4}\Delta G^{\ddagger}_{UN}+\Delta G^{\ddagger}_{NU}-\Delta G^{\ddagger}_{UN}, & x\in[x_5,+\infty],\end{cases} \quad \text{[S7]}$$

and with $x_1=x^{\ddagger}_{NI}$, $x_2=x_1+x^{\ddagger}_{IN}$, $x_3=x_2+x^{\ddagger}_{IU}$, $x_4=x_3+x^{\ddagger}_{UI}$, $x_5=x^{\ddagger}_{NU}$, $x_6=x_5+x^{\ddagger}_{UN}$, and $\beta=1/k_BT$. The analytical expressions of $G_1(x)$ and $G_2(x)$ are each connected piecewise cubic polynomials with connecting positions at the minima and maxima, as described in *Section IB*. In $G_0(x,y)$, the term $\Delta G^{\ddagger}_B e^{-c\left(\frac{x}{a}-1\right)^2-c\left(\frac{y}{b}-1\right)^2}$ introduces a barrier which is Gaussian-centered at (a, b) and separates the two pathways. The term $\left(\frac{y}{b}-1\right)^8$ provides a global constraint on the y coordinate.

Adopted parameter values are as follows: $a=3.25$ nm, $b=0.5$ nm, $c=6$ nm, $\Delta G^{\ddagger}_B=25\,k_BT$, $\Delta G^{\ddagger}_{NU}=17.5\,k_BT$, $\Delta G^{\ddagger}_{UN}=1.5\,k_BT$, $\Delta G^{\ddagger}_{NI}=15.5\,k_BT$, $\Delta G^{\ddagger}_{IN}=10.5\,k_BT$, $\Delta G^{\ddagger}_{IU}=18.0\,k_BT$, $\Delta G^{\ddagger}_{UI}=3\,k_BT$, $x^{\ddagger}_{NU}=2.5$ nm, $x^{\ddagger}_{UN}=3.5$ nm, $x^{\ddagger}_{NI}=2.0$ nm, $x^{\ddagger}_{IN}=1.2$ nm, $x^{\ddagger}_{IU}=1.3$ nm, and $x^{\ddagger}_{UI}=3.1$ nm. Note that the above parameters of the 2D landscape are not the ones to which the parameters extracted from the fit to the one-dimensional theory in Eq. **5** shall be compared. Rather, the parameters of the one-dimensional potential of mean force (they are listed as "true" in Table S3) should be used for validating the parameters extracted from the fit.

Stiffness of the pulling device $\varkappa=0.5$ pN/nm represented an optical trap. The corresponding Langevin equations are as follows:

$$\begin{aligned}\frac{dx}{dt}&=-\frac{D_m}{k_BT}\left[\frac{\partial G_0(x,y)}{\partial x}-\varkappa(X_0\pm Vt-x)\right]+\mathcal{R}_m(t),\\ \frac{dy}{dt}&=-\frac{D_m}{k_BT}\frac{\partial G_0(x,y)}{\partial y}+\mathcal{R}_m(t).\end{aligned} \quad \text{[S9]}$$

The effective diffusion coefficient $D_m = 2\times10^4$ nm^2/s was used both in the x and y directions.

Each stretching (relaxation) cycle began with the separation $X_0 = 0$ nm (50 nm) sufficiently small (large) such that N (U) was initially the predominantly populated state. One thousand force–extension curves were generated in each of the stretching and relaxation protocols at four nominal loading rates $\varkappa V = 0.1$, 1, 10, and 100 pN/s. The transition times and forces were recorded directly from the simulation.

II. Noisy Trajectories. Missed and Misjudged Events. Drift

A. Determining Transition Forces from Noisy Trajectories. The force–extension curves recorded in Brownian dynamics simulations of the system with an intermediate suffered, by design, from a low signal-to-noise ratio (Fig. 3*B*). As can be seen from Eq. **S3**, the extension X evolves in the combined potential of the worm-like chain linker and the pulling device, thus exhibiting a Boltzmann distribution with the SD $1/\sqrt{\varkappa+\varkappa_L}$, where the stiffness of the worm-like chain $\varkappa_L$ varies with force/extension. In the low-force region, $\varkappa_L \sim 0$ and the noise (the width of $\pm2\sigma$ interval) exceeds 2 nm in the extension and 10 pN in the force. In the high-force region, $\varkappa_L$ is large and the noise is reduced. Due to the worm-like chain nature of the linker, the amount of increase in the extension upon a transition is small at low forces compared with that at high forces, which makes it challenging to resolve the states and determine transition forces at low forces (below 30 pN).

To determine transition forces from noisy trajectories, we averaged $X(t)$ and $F(t)$ data from the simulation using an adaptive step size. The number of points to be averaged over was determined as follows. The force–extension curves were first fitted to the worm-like chain curve to find the mean values $\overline{F}_N(\overline{X}_N)$, $\overline{F}_I(\overline{X}_I)$, and $\overline{F}_U(\overline{X}_U)$, from which $\overline{X}_N(t)$, $\overline{X}_I(t)$, and $\overline{X}_U(t)$ were determined. When X is averaged over n points, the probability that the value of the extension $X(t)$ in state N makes an excursion over the mean value of the extension in state I at time t is approximately

$$p \sim \exp\left[-\frac{n(\varkappa+\varkappa_L)}{2}\left(\overline{X}_I(t)-\overline{X}_N(t)\right)^2\right], \qquad \textbf{[S10]}$$

where $\varkappa_L$ is the stiffness of the linker at the extension $\overline{X}_N(t)$. At high forces, the number of points to be averaged over was determined by setting $p \sim 10^{-6}$, which led to averaging the data over two points (note that the recorded data were already averaged over four points, so $n = 8$). At medium and low forces, n was determined by setting $p \sim 10^{-3}$, which led to $n \sim 200$ around 10 pN and $n \sim 20$ at 40 pN. Optimal choice of p was set by two factors: p that is too small usually leads to missed transitions because short-lived states are averaged away, and p that is too large usually leads to misjudged events, i.e., when a stochastic fluctuation in the extension is mistakenly interpreted as a transition. The averaged force–extension curves and extension–time curves exhibited three distinct states; transition forces and times were determined from these curves.

B. Missed and Misjudged Transitions. Missed and misjudged transitions primarily affect the transition force histograms [$P_{ij}(F)$ in Eq. **2**]: missed transitions at a force F lead to a decrease in the height of the bin corresponding to force F in the histogram, whereas misjudged transitions lead to an increase in the height of the corresponding bin. Because both missed and misjudged transitions are short-lived, their effect on the population [$N_i(F)$ in Eq. **2**] is generally negligible. Therefore, missed and misjudged transitions affect the rate map almost entirely through their effect on the histograms.

From the comparison of the transitions recorded by monitoring the molecular extension $x(t)$ with the transitions detected in the force–extension curves $F(X)$, missed and misjudged transitions were found to constitute 3–5% of the total transitions, and to be populated mostly in the low-force region. As the result, the rate map in Fig. 4*A* exhibited more scatter at low forces than the other two rate maps (Fig. 4 *B* and *C*), which came from data with a higher signal-to-noise ratio. Because of the effect of missed/misjudged transitions, the low-force region ($F \le 10pN$) on the rate map was excluded from the fit.

C. Effect of Baseline Drift. The effect of baseline drift was incorporated in the simulated transition force histograms by introducing Gaussian-distributed deviations to each transition force (6) and convolving the populations $\mathcal{N}(F)$ in each state with the same Gaussian distribution according to the following:

$$\tilde{\mathcal{N}}(F) = \int \frac{1}{\sigma_F\sqrt{2\pi}}\exp\left[-\frac{1}{2\sigma_F^2}\left(F-F'\right)^2\right]\mathcal{N}(F')dF'. \qquad \textbf{[S11]}$$

Values $\sigma_F = 1.6$ pN and $\sigma_F = 0.8$ pN were used for unfolding and refolding transitions, respectively, reflective of the fact that refolding transitions happen at relatively low forces where drift effect is relatively small.

III. Algorithm for Counting Trajectories in a Given State

Collecting the input $\mathcal{N}_i(F)$ in Eq. **2** (or "trajectories in state i at F" in Eq. **3**) can be automated through a simple algorithm. Let the state of interest be i, and all of the states directly connected to i be $\{j\}(j = 1, 2, \ldots, m)$. For any transition from state i to state j, the corresponding transition forces and transition times are $\mathcal{F}_{ij} = \{F_{ij}\}$ and $T_{ij} = \{t_{ij}\}$. $\mathcal{F}_{ij}$ and T_{ij} are arrays composed of individual transition forces F_{ij} and times t_{ij}, respectively, collected from all force–time trajectories at a given nominal loading rate. Similarly, the transition forces and times for the reversed transitions—from state j to state i—are $\mathcal{F}_{ji} = \{F_{ji}\}$ and $T_{ji} = \{t_{ji}\}$. Although the number of trajectories in a specific state can be found either from the transition forces or transition times, the nonmonotonic behavior of the force at the rip makes the algorithm in the time domain more convenient.

At a given time t, the average force experienced by the biomolecule in state i is $F = F(t)$. The number of trajectories that enter state i from state j can be found with the MATLAB function "sum" as sum($T_{ji} \le t$). Similarly, the number of trajectories that leave the state i to state j is sum($T_{ij} \le t$). The number of trajectories in state i at force F can then be found according to the following algorithm:

$$\mathcal{N}_i(F(t)) = \sum_{j=1}^{m}\left[\text{sum}\left(T_{ji} \le t\right) - \text{sum}\left(T_{ij} \le t\right)\right] + \mathcal{N}_i^0, \qquad \textbf{[S12]}$$

where $\mathcal{N}_i^0$ is the number of trajectories in state i at time $t = 0$.

Let us apply the above algorithm to the system with a single intermediate (Figs. 3 and 4*A*) to determine $\mathcal{N}_I(F = 30\,\text{pN})$, the number of trajectories in the intermediate (I) at force $F = 30$ pN. Data for this illustration are taken from 1,000 trajectories generated in the stretching protocol via Brownian dynamics simulations at the nominal loading rate $\varkappa V = 10$ pN/s. There are four types of transitions involved: $N \to I$ and $U \to I$ increase the number of trajectories in I, whereas $I \to N$ and $I \to U$ decrease the number of trajectories in I. The recorded transition times for each type of transition, $T_{NI} = \{t_{NI}\}$, $T_{IN} = \{t_{IN}\}$, $T_{IU} = \{t_{IU}\}$, and $T_{UI} = \{t_{UI}\}$, are listed in the boxes in Fig. S1. From the force–time trajectories, we find that the force $F = 30$ pN corresponds to the time $t = 9.92$ s at this loading rate. Transitions that occurred within the time interval from $t = 0$ s to $t = 9.92$ s are highlighted in gray in Fig. S1: among them are 2,127 $N \to I$ transitions, 1,777 $I \to N$ transitions, 17 $I \to U$ transitions, and 7 $U \to I$ transitions. Because the stretching protocol starts with all of the trajectories in the state N,

$\mathcal{N}_I^0 = 0$. Applying the algorithm in Eq. **S12**, we find the following: $\mathcal{N}_I(F = 30\,\text{pN}) = \mathcal{N}_I(t = 9.92\,\text{s}) = \text{sum}(T_{NI} \le 9.92\,\text{s}) - \text{sum}(T_{IN} \le 9.92\,\text{s}) - \text{sum}(T_{IU} \le 9.92\,\text{s}) + \text{sum}(T_{UI} \le 9.92\,\text{s}) = 2{,}127 - 1{,}777 - 17 + 7 = 340$.

IV. Standard Deviations of the Rates on the Rate Map

The transformation (Eqs. **2** and **3**) converts the mechanical fingerprints of a system into the rate map. To compute the SDs σ (Eq. **4**) of the force-dependent rates on the map, we first determine the SD of each component in the transformation: σ of the counts in the numerator and σ of the number of trajectories in a specific state in the denominator. Then, σ of the rate is calculated using the SE propagation method.

Because molecular transitions are affected by thermal noise from the environment, counts in each bin of the transition force histogram are subject to fluctuations. The fluctuating count in a given bin of the histogram satisfies the binomial distribution with the mean $n = N_c p$ and the variance $\sigma^2 = N_c p(1-p)$, where N_c is the total number of counts in the histogram and p is the probability that the transition force falls within this bin. The variance can be expressed in terms of n and N_c as $\sigma^2 = n(1 - n/N_c)$. For a specific bin with the measured count $P(F)\Delta F$, the corresponding variance is then $\sigma^2_{P(F)\Delta F} = P(F)\Delta F(1 - P(F)\Delta F/N_c)$, where the expected value n is replaced with the measured count $P(F)\Delta F$. Note that, due to reversible transitions ("hopping"), N_c can differ from the total number of trajectories.

Similarly, the number of trajectories in a specific state at force F is subject to fluctuations and satisfies the binomial distribution. For a state with the measured number of trajectories $\mathcal{N}(F)$, the corresponding variance is $\sigma^2_{\mathcal{N}(F)} = \mathcal{N}(F)(1 - \mathcal{N}(F)/N_t)$, where N_t is the total number of trajectories at the given nominal loading rate. In our simulations, $N_t = 10^3$.

The errors in the counts and the number of trajectories in a specific state propagate into the resulting rate through the SE propagation rule:

$$\begin{aligned}\sigma^2_{\ln(k(F))} &= \left[\frac{\partial \ln(k(F))}{\partial P(F)}\right]^2 \sigma^2_{P(F)} + \left[\frac{\partial \ln(k(F))}{\partial \mathcal{N}(F)}\right]^2 \sigma^2_{\mathcal{N}(F)} \\ &= \frac{\sigma^2_{P(F)}}{P(F)^2} + \frac{\sigma^2_{\mathcal{N}(F)}}{\mathcal{N}(F)^2} = \frac{\sigma^2_{P(F)\Delta F}}{(P(F)\Delta F)^2} + \frac{\sigma^2_{\mathcal{N}(F)}}{\mathcal{N}(F)^2} \\ &= \frac{1}{P(F)\Delta F} - \frac{1}{N_c} + \frac{1}{\mathcal{N}(F)} - \frac{1}{N_t}.\end{aligned} \qquad \textbf{[S13]}$$

with the quantities N_c, N_t, $P(F)\Delta F$, and $\mathcal{N}(F)$ defined as above. The correlation between the fluctuations in $P(F)\Delta F$ and $\mathcal{N}(F)$ is negligibly weak. Furthermore, $1/N_c + 1/N_t \ll 1/(P(F)\Delta F) + 1/\mathcal{N}(F)$ in most cases. We finally have

$$\sigma_{\ln(k(F))} \approx \left[\frac{1}{P(F)\Delta F} + \frac{1}{\mathcal{N}(F)}\right]^{\frac{1}{2}}. \qquad \textbf{[S14]}$$

It is worth pointing out that the SD $\sigma_{\ln(k(F))}$ computed above only accounts for the stochastic error. The systematic error in the measurement should be accounted for separately.

V. Expression for the Rate $k(F)$. Comparing Force-Clamp and Force-Ramp Data

The expression for the force-dependent rate $k(F)$ derived in ref. 7 strictly holds for a constant-force ("force-clamp") experiment. For this expression to be sufficiently accurate for a force-ramp experiment, the applied force $F = \varkappa(Vt - x)$ must be close to $F \approx \varkappa Vt$ throughout the transition over the barrier. This requires the well of the molecular potential to be much stiffer than the "spring" of the pulling device. Although the above requirement is usually satisfied for the transitions that originate from the folded state (i.e., unfolding) and "stiff" intermediates, it may not be satisfied for the transitions that originate from the "soft" unfolded state (i.e., refolding).

To trace back the first-order correction beyond $\varkappa Vt$ approximation, we first realize that there is a difference between the average force $\tilde{F}$ the molecule experiences while crossing over the barrier and the force F recorded as the transition force. The average force experienced during the transition is $\tilde{F} = \varkappa(Vt \mp \langle x\rangle_{\cup+\cap})$, where the end-to-end distance of the molecule is averaged over the well and the barrier regions $(\cup + \cap)$ of the potential covered by the transition. The minus $(-)$ and plus $(+)$ signs are for the forward and backward transitions, respectively. In contrast, the force recorded as the transition force is the average force experienced by the molecule just before the transition, $F = \varkappa(Vt \mp \langle x\rangle_{\cup})$, where the end-to-end distance is averaged over the well only $(\cup)$. The difference in $\langle x\rangle_{\cup+\cap}$ and $\langle x\rangle_{\cup}$ leads to the difference in the transition force experienced $\tilde{F}$ and recorded F.

It is a reasonable approximation to take $\langle x\rangle_{\cup+\cap} = x^{\ddagger}/2$ and $\langle x\rangle_{\cup} = \varkappa Vt/(\varkappa + \varkappa_m)$, where $x^{\ddagger}$ is the width of the barrier and $\varkappa_m$ is the curvature of the well of the molecular potential. The curvature $\varkappa_m$ can be expressed in a unified way in terms of the parameters on the molecular potential and the parameter ν controlling the shape of the potential: $\varkappa_m = 2\Delta G^{\ddagger}/[x^{\ddagger 2}(1-\nu)]$, where $\nu = 1/2$ corresponds to the harmonic-cusp and $\nu = 2/3$ to the linear cubic potential. We then have: $\tilde{F} = \varkappa(Vt \mp x^{\ddagger}/2)$ and $F = \varkappa Vt/[1 + (1-\nu)\varkappa x^{\ddagger 2}/(2\Delta G^{\ddagger})]$. The transition force experienced $\tilde{F}$ can now be expressed in terms of the transition force recorded F: $\tilde{F} = F[1 + (1-\nu)\varkappa x^{\ddagger 2}/(2\Delta G^{\ddagger})] \mp \varkappa x^{\ddagger}/2$. It is $\tilde{F}$ that mimics the role of the force in a force-clamp measurement; therefore, the expression for the rate in ref. 7 should be modified by replacing the force in the force clamp with $\tilde{F}$:

$$\begin{aligned}k\left(\tilde{F}(F)\right) = k_0 &\left[1 + \frac{\nu\varkappa x^{\ddagger 2}}{2\Delta G^{\ddagger}} \mp \frac{\nu F x^{\ddagger}}{\Delta G^{\ddagger}}\left(1 + \frac{(1-\nu)\varkappa x^{\ddagger 2}}{2\Delta G^{\ddagger}}\right)\right]^{\frac{1}{\nu}-1} \\ &\times \exp\left\{\Delta G^{\ddagger}\left\{1 - \left[1 + \frac{\nu\varkappa x^{\ddagger 2}}{2\Delta G^{\ddagger}} \mp \frac{\nu F x^{\ddagger}}{\Delta G^{\ddagger}}\left(1 + \frac{(1-\nu)\varkappa x^{\ddagger 2}}{2\Delta G^{\ddagger}}\right)\right]^{\frac{1}{\nu}}\right\}\right\}.\end{aligned} \qquad \textbf{[S15]}$$

Detailed analysis shows that the above correction works up to the first order of $\varkappa/\varkappa_m$, which allows the stiffness of the biomolecule to be as small as $\sim 5\,\varkappa$. With the typical spring constant of an AFM ~ 5 pN/nm and an optical trap ~ 0.3 pN/nm, and with an additional softening provided by the linker, the parameters of most biomolecules are in the region where the expression for the rate in Eq. **S15** is valid.

The above analysis shows what correction should be made when comparing the rates on the rate map (i.e., from force-ramp measurements) with the rates from constant force measurements. By converting the force F from the constant force measurements to $F' = (F \pm \varkappa x^{\ddagger}/2)/[1 + (1-\nu)\varkappa x^{\ddagger 2}/(2\Delta G^{\ddagger})]$, one can transfer the constant force rate $k(F)$ onto the rate map as $k(F')$. The plus $(+)$ and minus $(-)$ signs are for the forward and backward transitions, respectively. The reverse conversion should be made when the rate from the rate map is transferred to the constant force rate plot. For example, the slight deviation of the constant force rate from the rate obtained by transforming force-ramp data can be seen in Fig. S2*D* and could be corrected with the above conversion of the force.

VI. Fitting the Rates on the Rate Map

The force-dependent rates, represented by individual branches on the rate maps, along with their SDs, were fitted to Eq. **5** using Nonlinear Least Squares (Curve Fitting) function in MATLAB.

The location of the transition barrier, the barrier height, the intrinsic rate, and their corresponding SDs were extracted from the fit for each type of transitions. The fitting parameters for the system with a single intermediate are listed in Table 1. The fitting parameters for the other two, more complex, systems studied are listed in Table S2 (system with a cascade of barriers) and Table S3 (system with two competing pathways and an intermediate).

A competition between transitions originating from the same state, e.g., the forward transition $I \to U$ and the backward transition $I \to N$, limits the force range covered by the rates on the rate map for these transitions, which, in turn, increases the uncertainty in the fitting parameters. The effect is pronounced for the parameters of the barrier heights of backward transitions, such as $\Delta G^{\ddagger}_{IN}$, where the resulting SD obtained by the nonlinear least-square fitting is usually above 50% of its own value, invalidating such fitting parameters as unreliable. Instead of adopting the values extracted from the fit in such cases, we propose here a simple method of calculating the barrier heights for backward transitions based on the fitting parameters of its complementary transition. For two complementary transitions $i \to j$ and $j \to i$, Arrhenius equation gives $k^0_{ij} = A_{ij} e^{-\Delta G^{\ddagger}_{ij}}$ and $k^0_{ji} = A_{ji} e^{-\Delta G^{\ddagger}_{ji}}$. As these two complementary transitions share the same barrier, their effective diffusion coefficients are comparable (Eq. **S18**), so that $A_{ij} \approx A_{ji}$. We can now relate the barrier heights of these two transitions:

$$\Delta G^{\ddagger}_{ji} = \Delta G^{\ddagger}_{ij} + \ln k^0_{ij} - \ln k^0_{ji}. \qquad \textbf{[S16]}$$

The corresponding SD can be calculated based on the standard rule of error propagation:

$$\sigma^2_{\Delta G^{\ddagger}_{ji}} = \sigma^2_{\Delta G^{\ddagger}_{ij}} + \sigma^2_{\ln k^0_{ij}} + 2\,\mathrm{cov}_{\Delta G^{\ddagger}_{ij},\ln k^0_{ij}} + \sigma^2_{\ln k^0_{ji}}. \qquad \textbf{[S17]}$$

We apply the method developed in Eqs. **S16** and **S17** to calculate the values of the barrier heights and their SDs for the backward transitions $I_2 \to I_1$ and $I_3 \to I_2$ in Table S2 and $I \to N$ and $U \to I$ in Table S3.

As is mentioned in *Section IC*, in the case of two competing dissociation pathways, the parameters extracted from the fit should be compared with the parameters of the 1D potential of mean force $G^{PMF}(x)$ rather than with the parameters of the 2D landscape $G(x,y)$. To determine the potential of mean force along each of the two pathways, we blocked one pathway at a time and averaged out the y coordinate in the expression for the potential of mean force (8). The parameters of the potential of mean force along these two pathways are indicated as "true" parameters in Table S3.

Fitting parameters extracted from the additional test of the effect of the position dependence of the diffusion coefficient in *Section IA* are listed in Table S1. Force-dependent rates for this test were generated with the mean first-passage time equation (5),

$$k^{-1}(F) = \int_{\cup} \exp\left(-\frac{G_0(x) - Fx}{k_B T}\right) dx \int_{\cap} \frac{\exp\left(\dfrac{G_0(x') - Fx'}{k_B T}\right)}{D_m(x')} dx', \qquad \textbf{[S18]}$$

and fitted to Eq. **5**.

VII. The Limit of Independent Transitions

In the appropriate limit, when the topology of the landscape is such that the sequential transitions are independent, the transformation in Eqs. **2** and **3** reduces to a sequence of single-barrier transformations. An example of the free-energy landscape with a low, soft barrier followed by a higher barrier, along with the corresponding analysis, is shown in Fig. S2 (compare with Fig. 2).

1. Marko JF, Siggia ED (1995) Stretching DNA. *Macromolecules* 28(26):8759–8770.
2. Ermak D, McCammon JA (1978) Brownian dynamics with hydrodynamic interactions. *J Chem Phys* 69(4):1352–1360.
3. Berkovich R, et al. (2012) Rate limit of protein elastic response is tether dependent. *Proc Natl Acad Sci USA* 109(36):14416–14421.
4. Best RB, Hummer G (2010) Coordinate-dependent diffusion in protein folding. *Proc Natl Acad Sci USA* 107(3):1088–1093.
5. Zwanzig R (1988) Diffusion in a rough potential. *Proc Natl Acad Sci USA* 85(7):2029–2030.
6. Schlierf M, Berkemeier F, Rief M (2007) Direct observation of active protein folding using lock-in force spectroscopy. *Biophys J* 93(11):3989–3998.
7. Dudko OK, Hummer G, Szabo A (2006) Intrinsic rates and activation free energies from single-molecule pulling experiments. *Phys Rev Lett* 96(10):108101.
8. Dudko OK, Graham TGW, Best RB (2011) Locating the barrier for folding of single molecules under an external force. *Phys Rev Lett* 107(20):208301.

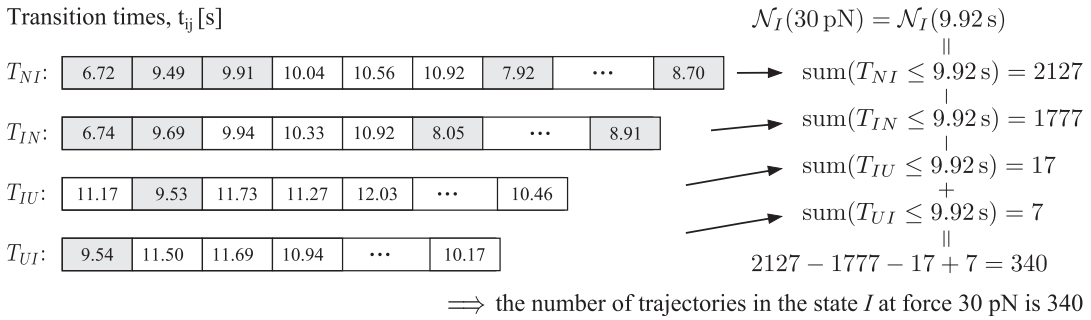

Fig. S1. Implementation of the algorithm in Eq. **S12** for counting trajectories in a specific state, illustrated with the system containing a single intermediate. The transition times for the transitions $N \to I$, $I \to N$, $I \to U$, and $U \to I$ are listed in the boxes next to T_{NI}, T_{IN}, T_{IU}, and T_{UI}, respectively. The force and the corresponding time of interest are $F = 30$ pN and $t = 9.92$ s. Transitions that occur within the time interval (0,9.92)s are highlighted in gray; the number of such transitions is indicated on the *Right* for each type of transition. The number of trajectories in state I at force $F = 30$ pN is found to be 340.

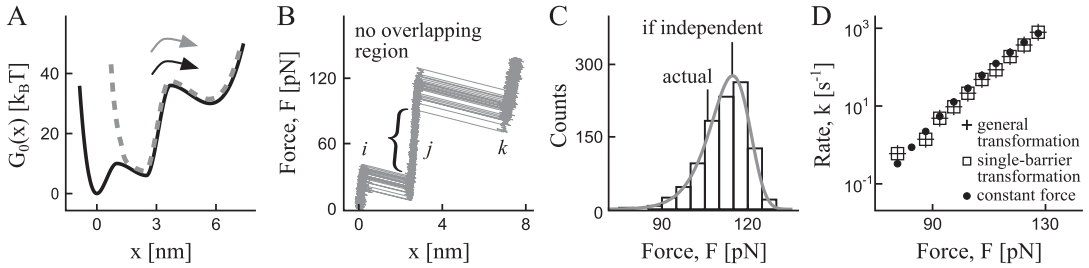

Fig. S2. Sequential unfolding transitions on a free-energy landscape with a low, soft barrier followed by a much higher barrier can be viewed as independent at high pulling speeds where backward transitions are rare. (*A*) Under a time-varying force, the transition over the second barrier on the potential in black is essentially equivalent to the transition on the potential in gray. (*B*) Force–extension trajectories generated on the black potential in A show no overlap between the forces faced upon arrival into the second well and the forces at the escape from this well. The brace indicates the nonoverlapping region separating the two clusters of the transition forces. (*C*) The rupture force distribution for the transition over the second barrier (black histogram) coincides with the distribution (gray curve) for this transition if it were independent from the transition over the first barrier. (*D*) The general transformation in Eqs. **2** and **3** (main text), applied to the transition over the second barrier, reduces to the single-barrier transformation. The resulting force-dependent rate is consistent with the rate obtained at constant force.

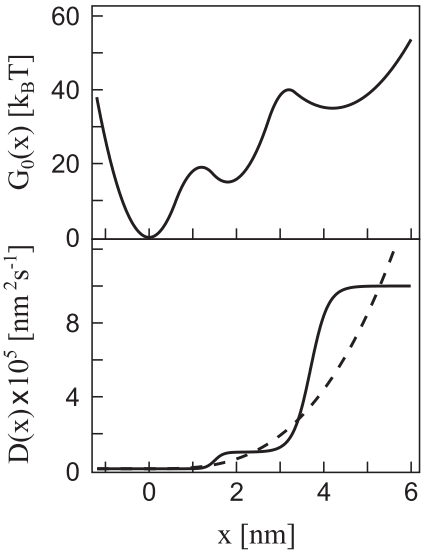

Fig. S3. Free-energy profile of the system with an intermediate (*Upper*) and the corresponding position-dependent diffusion coefficient (*Lower*).

Table S1. Parameters from the analysis of the system were $D_m(x) \propto x^3$ (dashed line in Fig. S3) with Eq. 5

Parameter set	$\ln(k_{NI}^0)$	$\Delta G_{NI}^{\ddagger}$	$x_{NI}^{\ddagger}$	$\ln(k_{IN}^0)$	$\Delta G_{IN}^{\ddagger}$	$x_{IN}^{\ddagger}$	$\ln(k_{IU}^0)$	$\Delta G_{IU}^{\ddagger}$	$x_{IU}^{\ddagger}$	$\ln(k_{UI}^0)$	$\Delta G_{UI}^{\ddagger}$	$x_{UI}^{\ddagger}$
True	−6.91	19.0	1.20	7.91	4.0	0.60	−10.58	25.0	1.40	8.82	5.0	1.00
Fit	−6.91	20.0	1.20	7.92	5.4	0.68	−10.52	26.2	1.41	8.82	6.0	1.08

Table S2. Intrinsic rates and barriers (heights and locations) from the analysis of the rate map in Fig. 4*B* with Eq. 5

Parameter set	$\ln\left(k^0_{NI_1}\right)$	$\Delta G^{\ddagger}_{NI_1}$	$x^{\ddagger}_{NI_1}$	$\ln\left(k^0_{I_1N}\right)$	$\Delta G^{\ddagger}_{I_1N}$	$x^{\ddagger}_{I_1N}$
True	−6.95	18.0	2.00	5.88	5.0	1.50
Fit	−6.80 ± 0.11	18.7 ± 1.5	2.01 ± 0.05	5.96 ± 0.12	6.5 ± 2.9	1.40 ± 0.07
	$\ln\left(k^0_{I_1I_2}\right)$	$\Delta G^{\ddagger}_{I_1I_2}$	$x^{\ddagger}_{I_1I_2}$	$\ln\left(k^0_{I_2I_1}\right)$	$\Delta G^{\ddagger}_{I_2I_1}$	$x^{\ddagger}_{I_2I_1}$
True	−5.79	17.0	1.40	5.39	6.0	1.20
Fit	−5.48 ± 0.19	16.8 ± 2.2	1.47 ± 0.07	5.49 ± 0.10	5.8 ± 2.3*	1.18 ± 0.05
	$\ln\left(k^0_{I_2I_3}\right)$	$\Delta G^{\ddagger}_{I_2I_3}$	$x^{\ddagger}_{I_2I_3}$	$\ln\left(k^0_{I_3I_2}\right)$	$\Delta G^{\ddagger}_{I_3I_2}$	$x^{\ddagger}_{I_3I_2}$
True	−7.94	19.0	1.60	6.69	4.0	1.50
Fit	−7.52 ± 0.36	18.5 ± 2.3	1.67 ± 0.12	6.82 ± 0.16	4.2 ± 2.5†	1.37 ± 0.09
	$\ln\left(k^0_{I_3U}\right)$	$\Delta G^{\ddagger}_{I_3U}$	$x^{\ddagger}_{I_3U}$	$\ln\left(k^0_{UI_3}\right)$	$\Delta G^{\ddagger}_{UI_3}$	$x^{\ddagger}_{UI_3}$
True	−10.07	20.0	2.00	6.89	2.0	2.50
Fit	−9.26 ± 0.50	19.2 ± 1.1	2.17 ± 0.15	7.12 ± 0.28	2.7 ± 1.2	2.20 ± 0.22

*$\Delta G^{\ddagger}_{I_2I_1} = \Delta G^{\ddagger}_{I_1I_2} + \ln k^0_{I_1I_2} - \ln k^0_{I_2I_1}$ and $\sigma^2_{\Delta G^{\ddagger}_{I_2I_1}} = \sigma^2_{\Delta G^{\ddagger}_{I_1I_2}} + \sigma^2_{\ln k^0_{I_1I_2}} + 2\mathrm{cov}_{\Delta G^{\ddagger}_{I_1I_2},\ \ln k^0_{I_1I_2}} + \sigma^2_{\ln k^0_{I_2I_1}}$.

†$\Delta G^{\ddagger}_{I_3I_2} = \Delta G^{\ddagger}_{I_2I_3} + \ln k^0_{I_2I_3} - \ln k^0_{I_3I_2}$ and $\sigma^2_{\Delta G^{\ddagger}_{I_3I_2}} = \sigma^2_{\Delta G^{\ddagger}_{I_2I_3}} + \sigma^2_{\ln k^0_{I_2I_3}} + 2\mathrm{cov}_{\Delta G^{\ddagger}_{I_2I_3},\ \ln k^0_{I_2I_3}} + \sigma^2_{\ln k^0_{I_3I_2}}$.

Table S3. Intrinsic rates and barriers (heights and locations) from the analysis of the rate map in Fig. 4*C* with Eq. 5

Parameter set	$\ln\left(k^0_{NU}\right)$	$\Delta G^{\ddagger}_{NU}$	$x^{\ddagger}_{NU}$	$\ln\left(k^0_{UN}\right)$	$\Delta G^{\ddagger}_{UN}$	$x^{\ddagger}_{UN}$
True	−9.94	19.7	2.84	5.38	3.1	3.45
Fit	−9.51 ± 0.12	18.5 ± 0.9	2.80 ± 0.07	5.46 ± 0.22	3.6 ± 1.2	3.43 ± 0.24
	$\ln\left(k^0_{NI}\right)$	$\Delta G^{\ddagger}_{NI}$	$x^{\ddagger}_{NI}$	$\ln\left(k^0_{IN}\right)$	$\Delta G^{\ddagger}_{IN}$	$x^{\ddagger}_{IN}$
True	−6.20	17.4	2.02	1.75	9.9	1.18
Fit	−6.12 ± 0.05	16.7 ± 1.4	1.96 ± 0.04	1.87 ± 0.18	8.7 ± 1.4*	1.27 ± 0.11
	$\ln\left(k^0_{IU}\right)$	$\Delta G^{\ddagger}_{IU}$	$x^{\ddagger}_{IU}$	$\ln\left(k^0_{UI}\right)$	$\Delta G^{\ddagger}_{UI}$	$x^{\ddagger}_{UI}$
True	−5.35	17.0	1.27	2.02	7.9	1.82
Fit	−5.19 ± 0.13	18.4 ± 4.0	1.31 ± 0.06	2.05 ± 0.34	11.1 ± 4.0†	2.11 ± 0.31

*$\Delta G^{\ddagger}_{IN} = \Delta G^{\ddagger}_{NI} + \ln k^0_{NI} - \ln k^0_{IN}$ and $\sigma^2_{\Delta G^{\ddagger}_{IN}} = \sigma^2_{\Delta G^{\ddagger}_{NI}} - \sigma^2_{\ln k^0_{NI}} + 2\mathrm{cov}_{\Delta G^{\ddagger}_{NI},\ \ln k^0_{NI}} + \sigma^2_{\ln k^0_{IN}}$.

†$\Delta G^{\ddagger}_{UI} = \Delta G^{\ddagger}_{IU} + \ln k^0_{IU} - \ln k^0_{UI}$ and $\sigma^2_{\Delta G^{\ddagger}_{UI}} = \sigma^2_{\Delta G^{\ddagger}_{IU}} + \sigma^2_{\ln k^0_{IU}} + 2\mathrm{cov}_{\Delta G^{\ddagger}_{IU},\ \ln k^0_{IU}} + \sigma^2_{\ln k^0_{UI}}$.